

ALMA and IRIS Observations of the Solar Chromosphere. I. An On-disk Type II Spicule

Georgios Chintzoglou^{1,2}, Bart De Pontieu^{1,3,4}, Juan Martínez-Sykora^{1,3,5}, Viggo Hansteen^{1,3,4,5}, Jaime Cruz de la Rodríguez⁶, Mikolaj Szydlarski^{3,4}, Shahin Jafarzadeh^{3,4}, Sven Wedemeyer^{3,4}, Timothy S. Bastian⁷, and Alberto Sainz Dalda^{1,5,8}

Lockheed Martin Solar & Astrophysics Laboratory, Palo Alto, CA 94304, USA; gchintzo@lmsal.com
 ² University Corporation for Atmospheric Research, Boulder, CO 80307-3000, USA
 ³ Rosseland Center for Solar Physics, University of Oslo, P.O. Box 1029 Blindern, NO-0315, Oslo, Norway
 ⁴ Institute of Theoretical Astrophysics, University of Oslo, P.O. Box 1029 Blindern, NO-0315, Oslo, Norway
 ⁵ Bay Area Environmental Research Institute, NASA Research Park, Moffett Field, CA 94035, USA
 ⁶ Institute for Solar Physics, Department of Astronomy, Stockholm University, AlbaNova University Centre, SE-106 91, Stockholm, Sweden
 ⁷ National Radio Astronomy Observatory, 520 Edgemont Road, Charlottesville, VA 22903, USA
 ⁸ Stanford University, HEPL, 466 Via Ortega, Stanford, CA 94305-4085, USA
 Received 2020 May 26; revised 2020 October 19; accepted 2020 November 2; published 2021 January 12

Abstract

We present observations of the solar chromosphere obtained simultaneously with the Atacama Large Millimeter/submillimeter Array (ALMA) and the Interface Region Imaging Spectrograph. The observatories targeted a chromospheric plage region of which the spatial distribution (split between strongly and weakly magnetized regions) allowed the study of linear-like structures in isolation, free of contamination from background emission. Using these observations in conjunction with a radiative magnetohydrodynamic 2.5D model covering the upper convection zone all the way to the corona that considers nonequilibrium ionization effects, we report the detection of an on-disk chromospheric spicule with ALMA and confirm its multithermal nature.

Unified Astronomy Thesaurus concepts: Solar chromosphere (1479); Solar chromospheric heating (1987); Solar electromagnetic emission (1490); Solar extreme ultraviolet emission (1493); Solar physics (1476); Solar radio emission (1522); Solar spicules (1525); Solar transition region (1532); Solar ultraviolet emission (1533)

1. Introduction

Chromospheric spicules were discovered in the 1870s in wide-slot spectroscopic observations in H α by A. Secchi (he called them in French petits filets, i.e., "little strings," or poils, i.e., "fur," due to their fine and slender appearance; Secchi 1877). We now know that spicules are jets of chromospheric material that are seen as rooted at the chromospheric network. A new class of spicules, termed "Type II spicules," was found a little over a decade ago in highresolution imaging observations taken at the Ca II H line (De Pontieu et al. 2007). These are more slender (apparent widths of $\lesssim 1''$) and exhibit higher plane-of-the-sky speeds (≈ 50 $-100 \,\mathrm{km \ s^{-1}})$ than their "traditional" counterparts. Their lifetimes differ, depending on whether we observe them in low chromospheric temperatures (e.g., in Ca II H, $\Delta t \approx 10$ –150 s) or in high chromospheric or transition-region temperatures (e.g., in Mg II h & k and $\Delta t \approx 3-10 \, \text{minutes}$; Pereira et al. 2014; Skogsrud et al. 2016). Type II spicules have been proposed to contribute to the heating of the corona based on observational studies (De Pontieu et al. 2009, 2011). This idea is challenged by lowresolution observations and simplified theoretical approaches (Klimchuk 2012; Tripathi & Klimchuk 2013; Patsourakos et al. 2014) but supported by recent high-resolution observations (Henriques et al. 2016; De Pontieu et al. 2017b; Chintzoglou et al. 2018) and numerical modeling (Martínez-Sykora et al. 2018). Martínez-Sykora et al. (2017) performed a 2.5D radiative magnetohydrodynamic (MHD) simulation (using the Bifrost code; Gudiksen et al. 2011) that considered the effects of ion-neutral interactions in the chromosphere, producing spicules that match the Type II properties mentioned above. Recently, several theoretical models have addressed the

problem of spicule formation, such as the 3D MHD simulation by Iijima & Yokoyama (2017), where a jet structure (matching the characteristic physical size and lifetime of Type II spicules) was produced and driven by Lorentz force.

There has been controversy regarding the nature of Type II spicules seen on-disk, which dates back to the first observations with the Interface Region Imaging Spectrograph (IRIS; De Pontieu et al. 2014): rapid brightenings along the length of the spicules suggest the upward shooting of hot chromospheric mass at plane-of-the-sky speeds as high as $\approx 300 \,\mathrm{km \ s^{-1}}$ (i.e., speeds greater than the highest plane-of-the-sky speeds of Type II spicules seen in Ca II H). Such events were termed "network jets" (Tian et al. 2014). Rouppe van der Voort et al. (2015) observed Type II spicules on-disk and found that the Doppler velocities associated with network jets are far lower than those seen on the plane of the sky (e.g., Tian et al. 2014). Advanced numerical modeling also suggests that network jets are often not manifestations of rapid mass flows but rather rapidly moving fronts of enhanced emission produced by the rapid dissipation of electric currents (e.g., De Pontieu et al. 2017b). In addition, unique observations from a Ly α rocket-borne spectroheliograph, i.e., the Very High Angular Resolution Ultraviolet Telescope 2.0 (VAULT2.0; Vourlidas et al. 2016), revealed a Type II spicule in Ly α (plasma temperatures of \approx 10,000–15,000 K) minutes before such network jets appeared in Si IV imaging (≈80,000 K) from IRIS (Chintzoglou et al. 2018). The same work by Chintzoglou et al. (2018) revealed unambiguously the multithermal nature of Type II spicules, since once the spicule appeared in transition-region temperatures, the structure persisted in Ly α imaging, even during moments of recurrent network jet brightenings.

The Atacama Large Millimeter/submillimeter Array (ALMA; Wootten & Thompson 2009) has recently become

available for the study of the chromosphere via imaging of free-free emission (from chromospheric electrons) in millimetric (mm) wavelengths. At mm wavelengths and under chromospheric conditions the source function, S_{λ} , of free-free emission is in local thermodynamic equilibrium (LTE), and so the source function is Planckian, $S_{\lambda} = B_{\lambda}(T)$:

$$S_{\lambda} = B_{\lambda} = \frac{2hc^2}{\lambda^5} \frac{1}{e^{hc/(\lambda k_{\rm B}T)} - 1} \tag{1}$$

where $k_{\rm B}$ is Boltzmann's constant, h Planck's constant, c the speed of light, T the blackbody temperature, and λ the wavelength of the observations. Since we are in the longwavelength limit $hc/(\lambda k_B T) = h\nu/(k_B T) \ll 1$, the equation above simplifies to the Rayleigh-Jeans approximation, which is a linear relationship of the source function to the blackbody temperature. Furthermore, the mm emission becomes optically thick over a rather narrow width of heights at any given observed line of sight (LOS) in the corrugated chromosphere. Since the emission is optically thick, we can use its brightness to determine the local plasma temperature (i.e., at the height of formation of the free-free emission). We thus define the "brightness temperature," $T_{\rm b}$, as the equivalent temperature a blackbody would have in order to be as bright as the observed emission, and consider it a measure of the local plasma temperature. Such measurements are enabled via interferometric imaging observations (at frequency ν) of the spectral brightness converted into T_b through the Rayleigh-Jeans approximation:

$$I_{\nu} \approx \frac{2k_{\rm B}\nu^2 T_{\rm b}}{c^2} = \frac{2k_{\rm B}T_{\rm b}}{\lambda^2}.$$
 (2)

However, since the chromosphere is fine-structured and corrugated, the local conditions producing the optically thick free-free emission can originate from quite a wide range of geometric heights; the formation height is also dependent on the electron density, and thus the actual height where the free-free emission becomes optically thick is typically not well known (Carlsson & Stein 2002; Wedemeyer-Böhm et al. 2007; Loukitcheva et al. 2015; Martínez-Sykora et al. 2020a). Rutten (2017) predicted that ALMA would observe fibrils along the canopy that are optically thick and thus would mask emission from lower heights. We further investigate the ALMA mm emission formation height problem in a companion publication (Chintzoglou et al. 2021, hereafter Paper II).

An interesting application of ALMA observations for the study of spicules was presented in the works of Yokoyama et al. (2018) and Shimojo et al. (2020), who focused on spicules seen at the limb (the latter group, however, captured a macrospicule). These studies faced challenges due to low signal-to-noise ratios (S/N) in ALMA limb observations (primarily due to an interferometric "knife-edge" effect when observing at the limb; Shimojo et al. 2017), also worsened by confusion/overlapping from foreground/background structures along the LOS, the latter being typical of observations of spicules at the limb.

In this study, we composed and analyzed a unique and comprehensive data set from joint observations with ALMA, IRIS, and the Solar Dynamics Observatory (SDO; Pesnell et al. 2012). Our data set is most appropriate for investigating the

rich dynamics of the solar chromosphere and transition region in plages and their peripheral areas. In particular this data set is excellent for the study of spicules thanks to the synergy of high spatial and temporal resolution spectral and imaging observations by IRIS with high time cadence and unique temperature diagnostic capabilities from ALMA interferometric observations.

This paper is organized as follows: in Section 2 we provide a description of the observations used in this work. In Section 3 we present an analysis of the observations and the synthetic observables, and in Section 4 we present our results, followed by a summary and conclusions in Section 5.

2. Observations

Our observations targeted a plage region in the leading part of NOAA Active Region (AR) 12651 on 2017 April 22, centered at heliographic coordinates N11°E17°, or at (x, y) = (-260'',265") in helioprojective coordinates (Figure 1(a)). The polarity of the photospheric magnetic field in that plage region was negative, i.e., of the same sign as the leading sunspot of NOAA AR 12651 (Figure 1(b)). The overall spatial distribution of the plage fields in the target appeared semicircular in shape, as organized around the outer boundary of a supergranule—the latter being made evident by the very low magnetic flux density in the core of the supergranule's area (Figure 1(b)). The common IRIS and ALMA field of view (FOV) contained part of that plage, including a photospheric pore, and also intersected the supergranular cell center, which appears in the chromosphere as a region of low background intensity (e.g., Figure 1(c)). The latter allowed us to study morphological structures, such as fibrils and loops, resolved in high contrast due to the weak background emission at the supergranular cell center.

ALMA is a general-purpose ground-based telescope located at an elevation of 5000 m in the Atacama Desert in Chile, operating in wavelengths ranging from 0.32 to 3.57 mm, or frequencies ranging from 84 to 950 GHz. It includes two arrays of antennas designed to perform Fourier synthesis imaging together or separately: (1) one array is composed of fifty 12 m antennas that can be moved to separations as large as 16 km; (2) the other array, the Atacama Compact Array (ACA), is a fixed array of twelve 7 m antennas designed for interferometry plus four 12 m total power (TP) antennas (see below). ALMA was commissioned for solar observing in 2014–2015 and was first made available to the community for scientific observations in 2016 (see Wedemeyer et al. 2016; Shimojo et al. 2017; White et al. 2017). Solar observations use both the 50-antenna 12 m array and the ACA 7 m array as a single array. The 50antenna array was only available in the most compact ALMA antenna configurations (C43-1, C43-2, and C43-3) in 2016–2017 (Shimojo et al. 2017). In addition, pending ongoing commissioning activities, solar observations were initially only available at 3 mm (100 GHz; Band3) and at 1.25 mm (239 GHz; Band6). The observations reported here used the ALMA C43-3 antenna configuration, which provides antenna separations ranging from 14.6 to 500 m. The ACA 7 m antennas provide antenna spacings ranging from 8.7 to 45 m. They were used to image the plage region with an angular resolution of $\approx 0.98 \times 0.97$ as determined by the synthesized beam. The array configuration and the beam aspect are summarized in Figure 2. It is important to note, however, that any interferometric array acts as a spatial filter. It does not

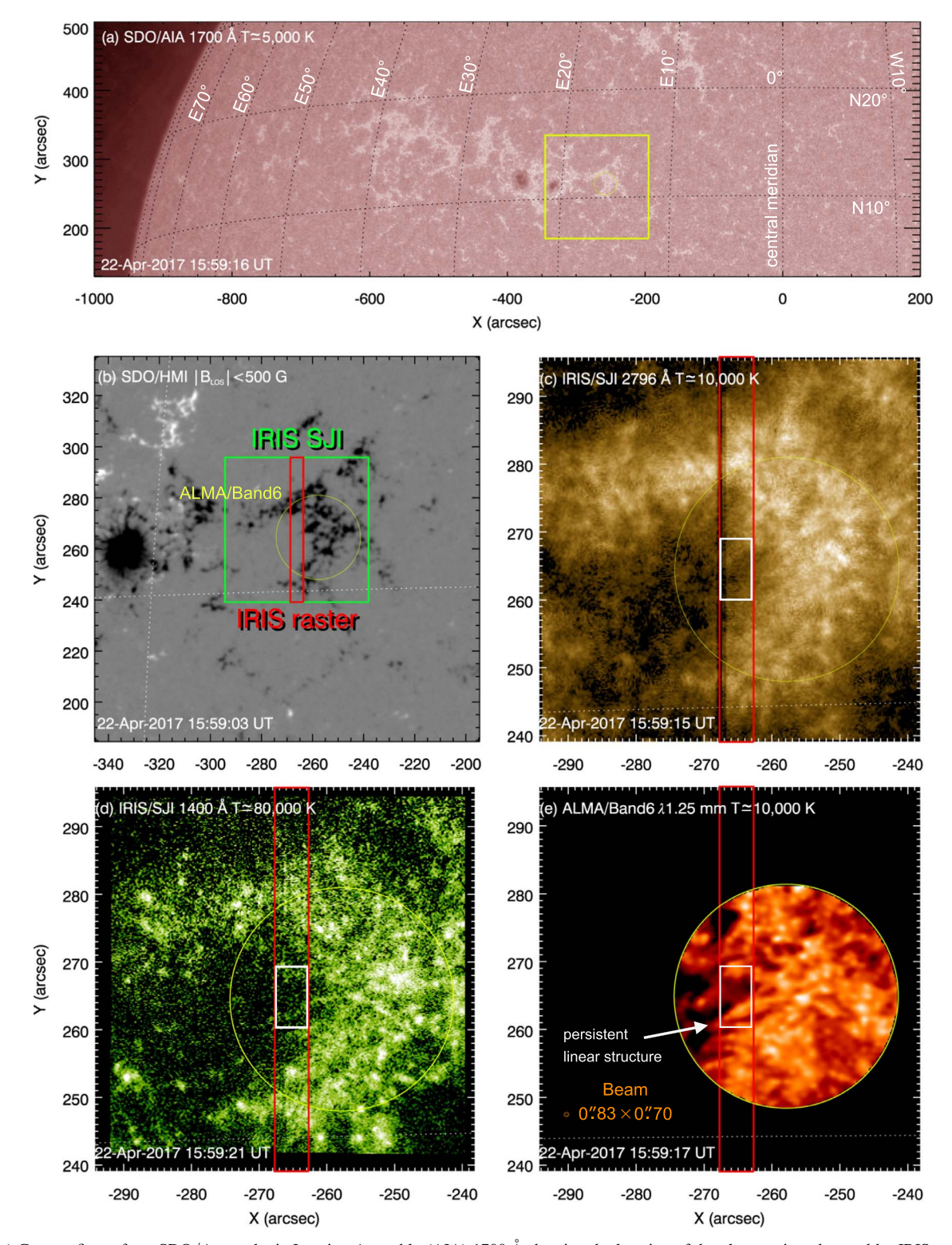


Figure 1. (a) Context figure from SDO/Atmospheric Imaging Assembly (AIA) 1700 Å showing the location of the plage region observed by IRIS and ALMA. (b) The magnetic field distribution from SDO/Helioseismic Magnetic Imager (HMI) is shown for the boxed area in panel (a). The same panel contains a narrow-width inset plot of IRIS/"slit-jaw" context imaging (SJI) 2832 Å (Mg II continuum). (c) Mg II 2796 Å and (d) Si IV 1400 Å corresponding to the IRIS/SJI FOV (green box) in panel (b). The corresponding ALMA/Band6 FOV is shown in panel (e). The white rectangle marks the FOV of the raster cutout shown in Figure 3 (i.e., the raster trimmed along the y-direction to focus on the spicule; note the persistent linear-like structure near the future location of the spicule).

measure spatial frequencies lower than the minimum antenna separation in the array, corresponding to the largest angular scales in the source. For the Sun, most of the power is on the largest angular scales, and it is therefore important to recover them if photometry is required for the science goals. The 12 m

TP antennas provide this information by mapping the full disk of the Sun with an angular resolution corresponding to that of a 12 m antenna (note that usually, and in our observations, only one TP antenna was used). Roughly speaking, TP maps provide measurement on angular scales of >24", and the joint

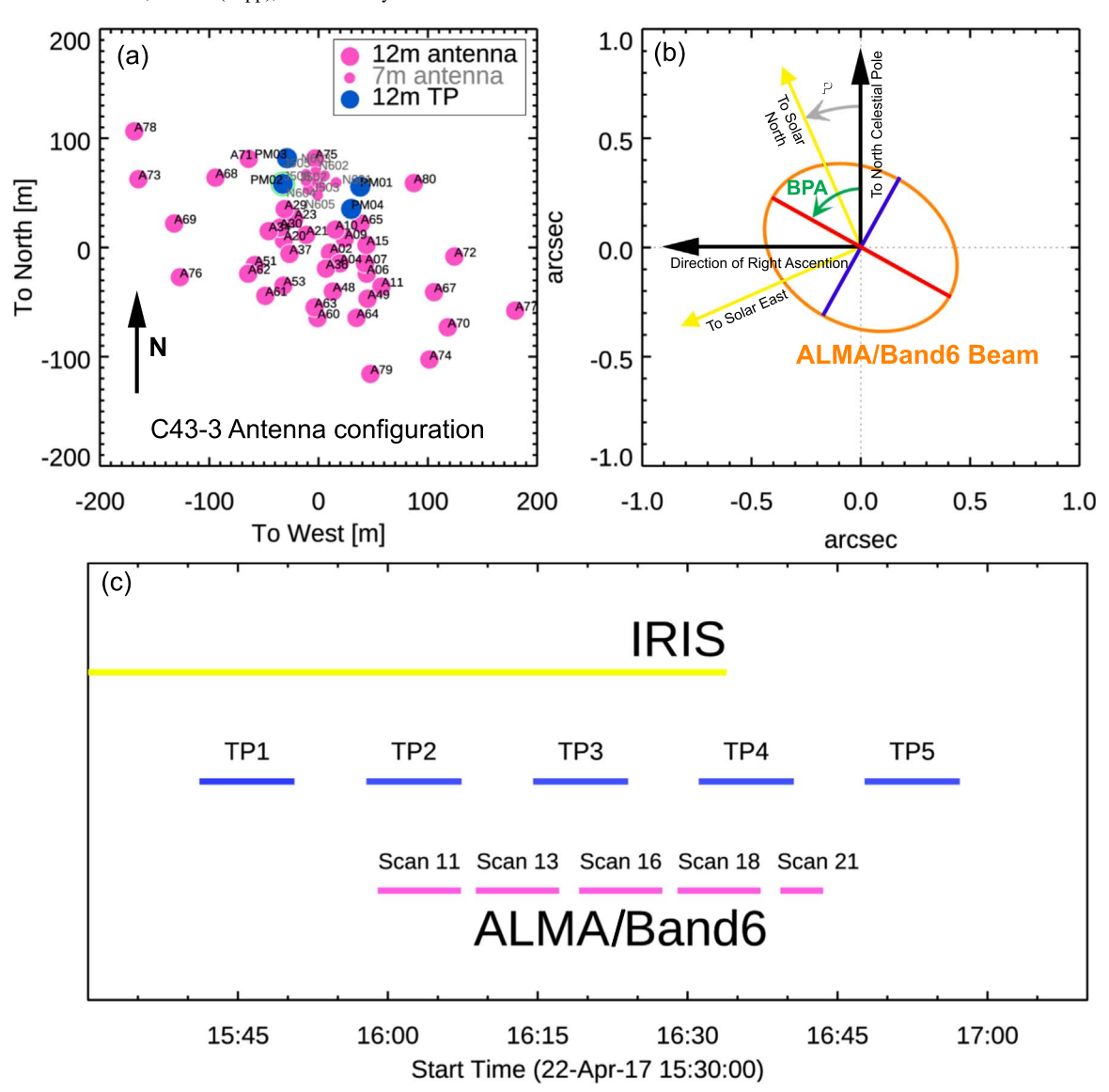


Figure 2. (a) ALMA antenna configuration at the time of the observations. Three out of forty-three 12 m array antennas were excluded due to problems with their calibration; similarly, only nine antennas in the 7 m array were included. For the TP measurements only one 12 m TP antenna was used (highlighted with a green circle). The labels correspond to the specific identification name of each antenna. (b) The resolution element in the interferometric imaging (i.e., the "beam") is a 2D Gaussian FWHM with a major (red) and minor (blue) axis. The beam's position angle is measured between the north celestial pole and the beam major axis counterclockwise, like the solar position angle. Note that the solar position angle at the time of the observations was negative, i.e., $\approx -25^{\circ}$. (c) Timeline of joint ALMA/Band6 and IRIS observations. Scans were interrupted by special scans (not shown) required for calibrations of the interferometric array.

 $12\,\mathrm{m/ACA}$ array provided measurements on angular scales of <24'' for the Band6 observations reported here. The two types of measurements were combined in postprocessing using the "feathering" technique (e.g., Cotton 2017).

IRIS is a spaceborne imaging spectrograph operating in nearultraviolet (NUV) and far-ultraviolet (FUV) wavelengths, designed to improve our understanding of the solar chromosphere and transition region. It produces two types of observations: (1) SJI in passbands centered at Mg II k 2796 Å, C II 1330 Å, Si IV 1400 Å, and Mg continuum 2832 Å and (2) spectral raster scans (in short, rasters), the latter covering passbands containing several chromospheric and transition-region lines found within NUV and FUV spectral windows (range 2783–2834 Å for NUV and two ranges, 1332–1358 Å and 1389–1407 Å, for FUV). The rasters are produced at a variety of slit sampling positions, giving a choice of dense (0."35 steps), sparse (1"), or coarse (2") rasters

in lines like Mg II, Si IV, C II, etc. IRIS provided coordinated observations with ALMA on 2017-04-22 13:29:36 UT until 16:33:53 UT. The IRIS observing mode for this data set was OBS 3620502035, producing SJI images at the aforementioned passbands at 0.16 pix⁻¹ with an FOV of $60'' \times 65''$ at 13 s cadence and also 16-step dense rasters (i.e., 0."35 steps in the helioprojective x-direction and 0."16 in y across the slit) covering $5'' \times 60''$ at 26 s cadence of an area intersecting the plage, a photospheric pore, and the core of the supergranule (red rectangle in Figures 1(b)-(d)). The spectral resolution in the rasters was 0.0256 Å for the NUV window and 0.053 Å for the FUV. Since the exposure time was 0.5 s in order to optimize raster cadence for Mg II k spectra, the 1400 Å SJI images show low signals and have been summed, using threeframe ("boxcar") temporal averaging on the image series. Such averaging improved the S/N enough to resolve dynamic features (at an effective timescale of 39 s). Unless otherwise

Onset of Growth of Linear-like Structure (Type-II Spicule)

Time of "Network Jet" Occurrence

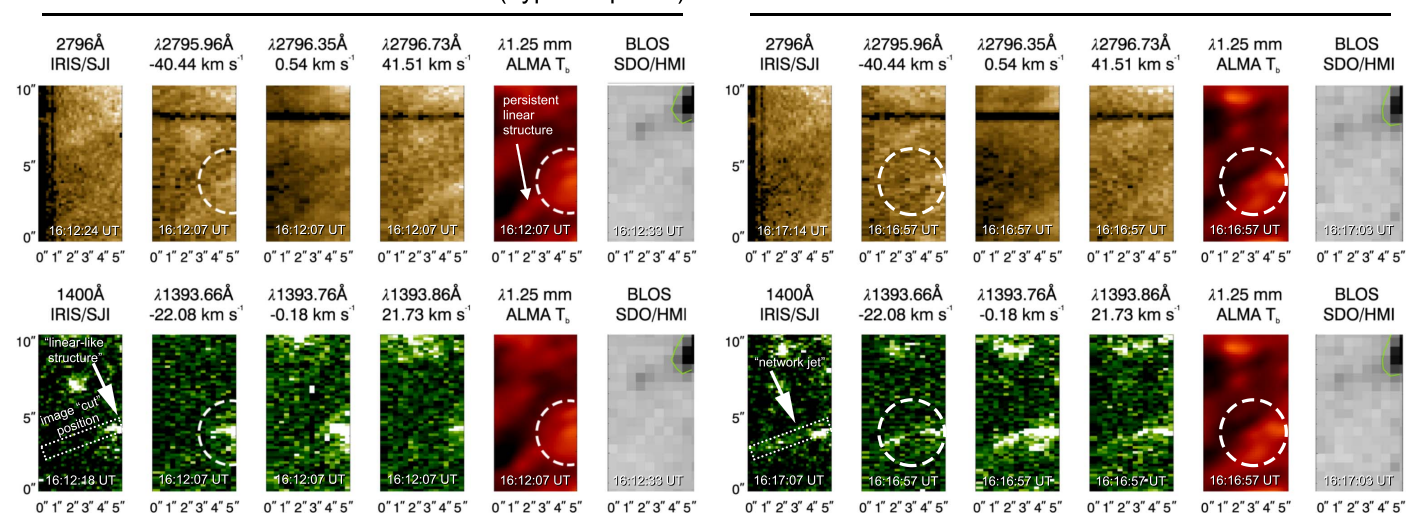


Figure 3. Intercomparison of IRIS and ALMA/Band6 observations at two different times in the evolution of the linear-like structure. Raster scans are shown at selected wavelength positions in Mg II (top) and Si IV (bottom), showing the clear appearance of the rapidly evolving structure in Mg II and Si IV (dashed circles). In the 1400 Å IRIS/SJI panels we show the position of the image cut we performed on each observable to produce Figure 5. In the panels with SDO/HMI magnetograms (scaling clipped at ± 250 G) we overplot an isocontour of ± 100 G.

specified in this paper, we did not perform temporal averaging on the raster data since they were of higher S/N.

ALMA observed in Band6 from 15:59 UT to 16:38 UT and produced five scans of the target region, owing to four breaks for interferometric calibration (spanning 1.75 to 2.25 minutes; Figure 2(c)). In addition, ALMA observed in Band3 between 17:20 UT and 17:56 UT but without IRIS support. Thus, the overlapping time range between ALMA and IRIS amounts to a total of 34 minutes of Band6 data (Figure 2; Band3 not shown). Within this period of time, ALMA was able to capture in ultrahigh cadence (2 s) the rich dynamic activity and interesting evolution of linear-like structures, including indications of shocks in the region just above the plage (we address this in a separate publication, Paper II). In this work, we focus on a slender and dynamically evolving linear-like structure (Section 4) resolved with ALMA/Band6 observations at high cadence and spatial resolution.

3. Analysis

3.1. Reduction of ALMA and IRIS Observations

The calibrated ALMA data was obtained from the ALMA Science Archive and processed with the Solar ALMA Pipeline (SoAP; M. Szydlarski et al. 2020, in preparation; see also Wedemeyer et al. 2020 for details). SoAP is developed by the SolarALMA project in Oslo in collaboration with the international SolarALMA development team and is based on the Common Astronomy Software Applications (CASA) package (McMullin et al. 2007).

Imaging with SoAP uses the multiscale (multifrequency) CLEAN algorithm (Rau & Cornwell 2011) as implemented in CASA, self-calibration for a short time window of 14 s, primary-beam correction, and combination of the interferometric data with the TP maps via the feathering method. For the Band6 observations reported here, the TP maps were scaled to a mean quiet Sun brightness of 5900 K as recommended by White et al. (2017), who cited a nominal uncertainty of 5%. For the interferometric part, all frequency channels are used to produce one continuum image for each time step at 2 s cadence.

The final result is a time sequence of absolute brightness temperature continuum maps at 2 s cadence with short ($\sim 2 \text{ minutes}$) calibration breaks that divide the sequence into 10 minute segments or "scans."

Ensuring precise co-registration of the feathered ALMA/Band6 interferometric maps with the IRIS rasters is imperative for the successful analysis of this comprehensive data set. For this purpose, we used imaging observations in 1700 Å from the AIA (Lemen et al. 2012) on board SDO to coalign IRIS/SJI 1400 Å and 2796 Å and FUV/NUV raster image series with other SDO observations, such as LOS magnetograms produced with the HMI (Scherrer et al. 2012). To coalign ALMA with IRIS, we exploited the very high degree of similarity between morphological structures seen in ALMA/Band6 maps and IRIS/SJI 1400 Å images. This can be readily seen in Figure 1, e.g., by comparing bottom panels (d) and (e) for bright structures in the plage region. We address the origin of this interesting similarity in Paper II.

3.2. General Morphology of the Structure Seen in IRIS and ALMA/Band6 Observations

The IRIS-ALMA FOV captured several slender linear-like structures; some of them appeared as persistent and slowly evolving structures, while others showed dynamic behavior over the duration of the observations. In Figure 3 we present a dynamic and prominent linear structure when it first appeared at around 2017 April 22 16:12 UT in the western part of the IRIS raster FOV (e.g., see the left group of panels in Figure 3; structure in IRIS/SJI 1400 Å panel indicated by an arrow; for a movie see electronic version of Figure 1 in Paper II). Over the minutes that followed, this structure grew from west to east (e.g., see right group of panels in Figure 3 around 16:17 UT; structure indicated by an arrow). We focus our study on the aforementioned dynamic linear structure in Figure 3 since (1) its outstanding dynamic nature is interesting and because (2) for most of its time evolution it is observed against low background emission (due to the supergranular core's weak magnetic fields; SDO/HMI panels in Figures 1 and 3), with the

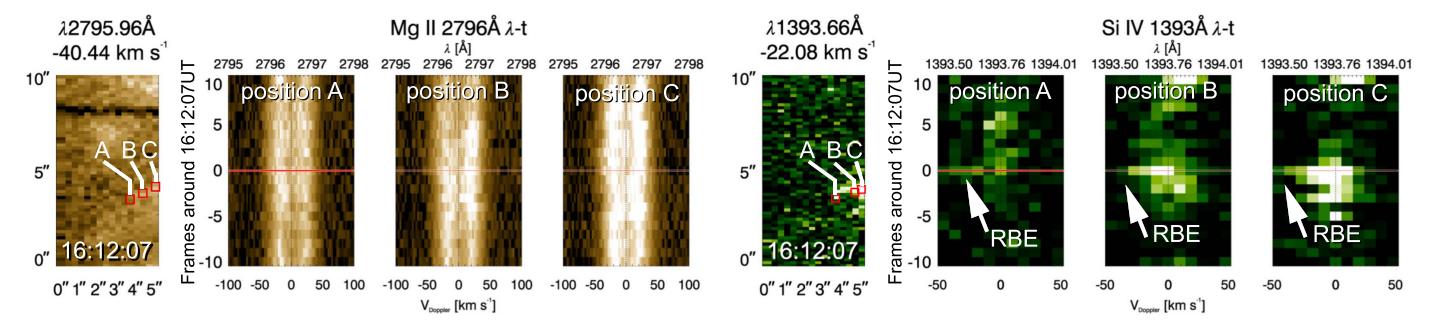


Figure 4. λ -t plots for Mg II and Si IV at three different positions along the linear structure (shown in Figure 3 at 16:12 UT), illustrating the RBE nature of the structure with speeds of -50 km s^{-1} (arrow in Mg II λ -t; speeds in excess of -50 km s^{-1} for Si IV). See text for discussion.

latter allowing us to take measurements that are free of confusion from background structures.

Previous studies on the on-disk counterparts of Type II spicules have identified them through signatures like shortlived asymmetries of chromospheric/transition-region spectral lines, which render the lines skewed to the blue or red wing. This effect is described as a "rapid blueshifted excursion" (RBE) or "rapid redshifted excursion" (e.g., Langangen et al. 2008; Rouppe van der Voort et al. 2015). Here, by exploring the spectral information in the IRIS raster series at the corresponding time in the SJI maps of 16:12 UT in Figure 3, we can see that the structure appears faintly in the raster images at the blue wing of the Mg II k line, corresponding to Doppler blueshifts of $-40 \,\mathrm{km \ s^{-1}}$, and also in the Si IV 1393 Å line, here seen clearly at $-22 \,\mathrm{km \ s^{-1}}$ (see rasters in left group of panels in Figure 3; dashed semicircles in Mg II k and Si IV rasters and in ALMA/Band6 common FOV). The structure is not clearly seen in line positions that correspond to Doppler redshifts as high as the blueshifts (see Figure 4 for λ -t plots sampling the structure at three different positions across its length). While the evidence is clear in Si IV, Mg II also shows such signatures at least in "position B," albeit with low S/N. As a result we conclude that this feature can be characterized as an RBE event. The fact that such a slender structure exhibits the spectral signatures of an RBE event further suggests that the linear-like structure is the on-disk manifestation of a Type II spicule shooting mass upward (blueshifts of \approx -50 km s⁻ typical of RBEs associated with Type II spicules; Rouppe van der Voort et al. 2015; De Pontieu et al. 2017b). Later on, the structure grows further to the east and brightens along its length in Si IV (right group of panels in Figure 3 at 16:17 UT). Throughout the evolution of the linear structure, in the ALMA/ Band6 data it appears somewhat wider and shorter as compared to its appearance in the blue wing of Mg II k and in Si IV. However, considering that ALMA/Band6 and IRIS/Mg II k observations probe similar ranges of temperatures (e.g., Bastian et al. 2017), such differences in morphological structures between Mg II k and ALMA/Band6 could also be due to the difference in spatial resolution between IRIS data (0."35 pix⁻¹ in x and 0.16 pix⁻¹ in y) and ALMA/Band6 data (here, beam size is ≈ 0.77 at best). Another possibility, despite the common ranges of temperatures in both observables, is that we may not be looking at the same part of the structure as the observed intensities may be coming from different parts of the same multithermal event (we address this in Paper II). In Si IV rasters, different parts of the structure can be seen clearly at -22 km s^{-1} and at $+22 \text{ km s}^{-1}$ away from the line center, although the signal in those line positions is lower than that at the line core.

3.3. Dynamic Evolution of the Type II Spicule

In order to properly study the dynamics, we proceeded by making an image "cut" in the raster series aligned along the principal axis of the spicule (i.e., its longest spatial dimension; position of cut shown in Figure 3 1400 Å SJI panels only for reference as here we focus on the raster series) and producing a spacetime plot (hereafter referred to as an "x-t plot"). For our ALMA/Band6 observations we made an x-t plot of the brightness temperature, $T_{\rm b}$. For IRIS Mg II k and Si IV we produced x-t plots in selected wavelength positions sampling the spectral lines around their rest positions, and we stacked these x-t plots sorted in the velocity space as shown in Figure 5 (a red line marks the time of the frames in Figure 3). In the same figure, we also show IRIS Mg II k and Si IV x-t plots after integrating the rasters in wavelength (within 0.7 Å and 0.2 Å of the line rest positions, respectively). We highlight the parabolic x-t profile of the spicule with yellow dotted lines in Figure 5. The parabola was extracted from the Si IV wavelengthintegrated x-t envelope and replicated and overplotted in selected panels of the other observables to serve as a guide for comparisons. The integrated Si IV shows a parabolic profile in a more complete way. In comparison, the profiles in specific wavelength positions appear partial, albeit consistent with Doppler shift modulation due to ascending and descending plasma motions along the evolution timeline. On the other hand, the integrated Mg II x-t profile shows a less clear picture, as we discuss below. Mg II is a complex spectral line that is typically optically thick and formed under non-LTE conditions. Disk counterparts of spicules appear as features that can be brighter or darker than neighboring features during their complex temporal evolution (e.g., Rouppe van der Voort et al. 2015; Bose et al. 2019). This complex evolution is a key reason for the lack of clear parabolic evolution compared to that seen in Si IV. The structure initially grows from west to east in both the ALMA/Band6 and IRIS raster plots in Figure 3.

At first glance, the integrated intensities between the Si IV and Mg II k x–t plots appear anticorrelated in these structures: Si IV seems to be brightest where Mg II is darkest (dotted circles in Figure 5; compare the intensity in the x–t plots between times 16:15 and 16:20 UT; there seems to be an intensity depression in Mg II x–t). This can be understood as cool material being injected into the corona (i.e., the spicule) with its bulk appearing in absorption in Mg II and its interface with the corona seen in emission in transition-region temperatures (i.e., Si IV). We present this interpretation in detail by carefully investigating the similarities and anticorrelations of intensities between different observables in

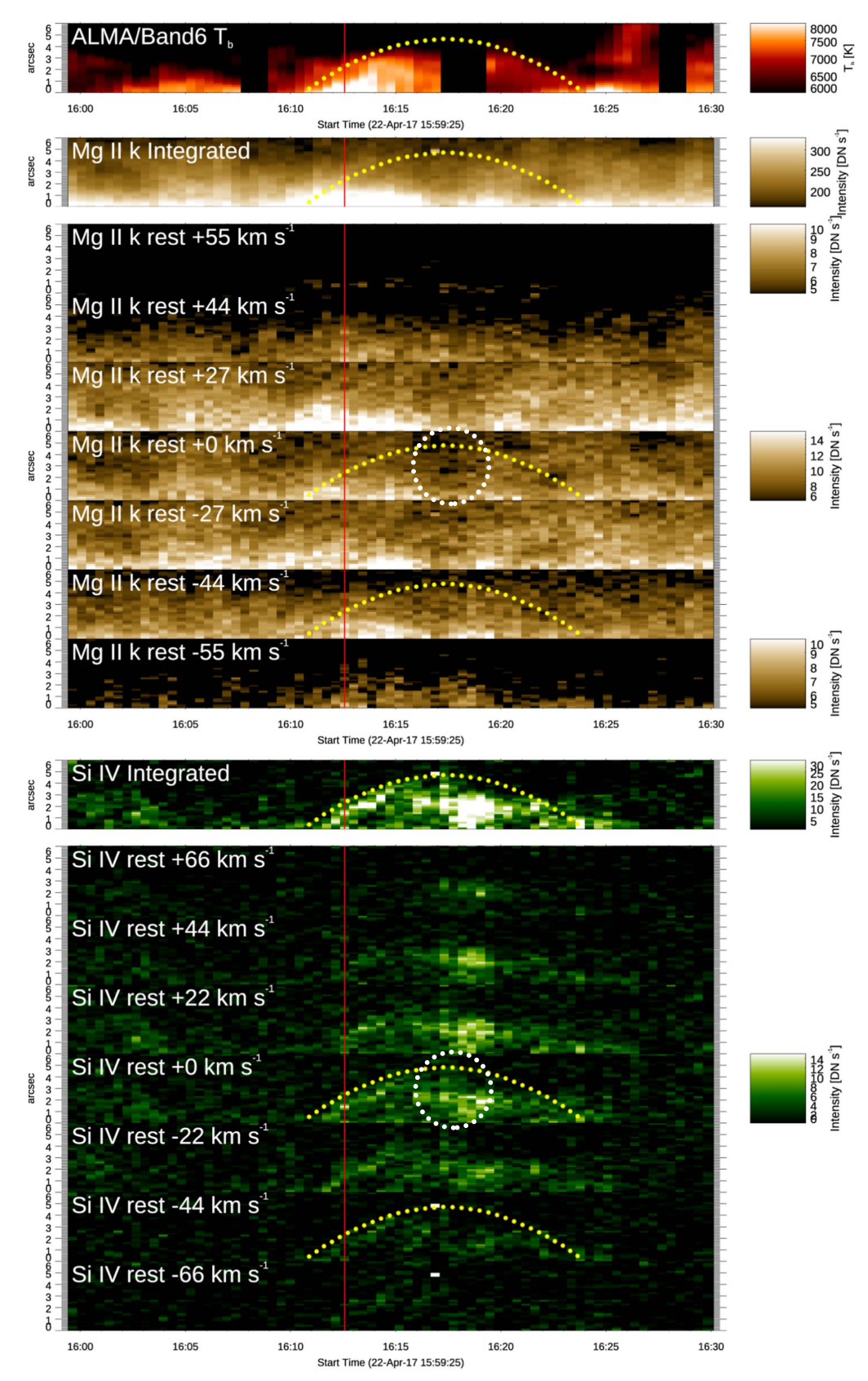


Figure 5. ALMA/Band6 and IRIS raster x—t plots for the linear-like structure shown in Figures 3 and 4. For IRIS the stack of x—t plots is arranged in the velocity space as annotated, centered about the rest wavelengths of Mg II k (middle) and Si IV (bottom), in addition to x—t for wavelength-integrated rasters. The western side of the cut in Figure 3 is at the bottom of the x—t plots. Note the clear parabolic trace in ALMA/Band6 and the wavelength-integrated Si IV x—t. Also note the enhanced absorption (dotted circle) in Mg II, which alters the appearance of a full parabolic profile. Due to low photon counts in x—t for Mg II at ± 55 km s⁻¹ we reduce the dynamic range as shown in the respective color bars. The red vertical line denotes the time of observations shown in Figure 4. See text for discussion.

Paper II. In order to interpret this behavior properly, we compare our observations to our synthetic observations (see next section). First of all, these three observables represent very different properties of the plasma, i.e., ALMA/Band6 provides brightness temperature at an unspecified height, Mg II intensity comes from radiation that is optically thick (chromosphere), and Si IV intensity comes from radiation that is optically thin (transition region). It is also interesting that Mg II k does not reach the parabola as close as ALMA/Band6 does. Si IV, on the other hand, is contained under the parabola rather well, also hosting transient brightenings (bright areas associated with the network jet).

However, overall, the behavior seen between these observables is quite similar—for instance, compare the parabolic profiles in the x-t plots of Mg II rest ± 27 km s⁻¹ and ALMA/Band6, where the trace of the ALMA/Band6 emission seems to be co-temporal with similar intensity enhancements in Mg II k (i.e., between 16:12 and 16:14 UT), but not beyond those, where Mg II k does not seem to extend as high as ALMA/Band6. We also note that at Mg II rest -55 km s⁻¹ the profile in x-t is more pronounced than that at +55 km s⁻¹, which is a manifestation of the spicule's RBE nature. In fact, the Mg II rest -55 km s⁻¹ profile's duration and elongation corresponds relatively well to the x-t profile in ALMA/Band6 up until \sim 16:19 UT (the gaps in the ALMA/Band6 observations were due to breaks for calibration purposes).

The Si IV x-t plots (Figure 5; green-colored plots) suggest upflows in the spicule during its ascent (or "growth phase"), which are then followed by downflows (the "receding phase"). The ascending part of the parabolic profile is quite localized (appearing as a bright thin trace) and is seen clearly in the blue wing (even at blueshifts as high as $-66 \,\mathrm{km \ s^{-1}}$). At around 16:16-16:17 UT, a network jet brightening occurs in the spicule (dotted circle in Figure 5) with an apparent (i.e., projected on the plane of the sky) speed of \approx 95 km s⁻¹. Since the time cadence of the rasters is 26 s, this apparent speed is only a lower limit. We note that the network jet brightening starts just after the x-t profile's "apex" point, and it is best seen in redshifts, which is consistent with mass motions moving away from the observer. An alternative explanation could be that the spicular column is curved with respect to our LOS. We should also note, however, that the Si IV integrated intensity appears to come just above the instantaneous maximum extent of ALMA/Band6, at least before the onset of the network jet brightening (where we do not have ALMA/Band6 data). We further illustrate this fine point in the following sections.

3.4. Bifrost Simulation of Type II Spicules and Synthesis of ALMA and IRIS Observables

In order to further investigate the nature of the Type II spicule, we employed a 2.5D MHD numerical model based on the Bifrost code (Gudiksen et al. 2011) covering the upper solar convection zone all the way to the low corona (extending up to 40 Mm from the photosphere). This model includes the effects of nonequilibrium (NEQ) ionization (for hydrogen and helium; Leenaarts et al. 2007; Golding et al. 2016) and ambipolar diffusion (Martínez-Sykora et al. 2017; Nóbrega-Siverio et al. 2020). Martínez-Sykora et al. (2020b) compared this model with an equivalent model without NEQ ionization in LTE conditions. The most important difference for the matter of interest of this paper is that the NEQ ionization increases the electron density, $N_{\rm e}$, in the upper chromosphere due to the large

recombination timescale. In addition, any heating (for instance, due to ambipolar diffusion) or cooling (i.e., due to adiabatic expansion) will increase or decrease the temperature instead of ionizing or recombining the plasma owing to large ionization/ recombination timescales producing multithermal structures, such as Type II spicules or low-lying loops. As we discuss later, this improves the agreement between the synthetic observables and the observations (e.g., as compared to that in Martínez-Sykora et al. 2017). The spatial scale in the simulation was 14 km (grid point)⁻¹. We stored the output of the model at a cadence equivalent to 10 s of solar time. After the simulation relaxed from the initial condition (which took \approx 50 minutes of solar time), the remaining total duration of the simulation we analyze here represented ≈10 minutes of solar time. Using this 2.5D model output, we synthesized observables from the physical conditions in the Bifrost model (for each snapshot of the simulation) that correspond to the observed chromospheric emission from a vantage point overlooking the simulation from the top of the domain, essentially simulating "sit-and-stare" slit observations near the solar disk center.

The simulation produced Type II spicules in several locations in the computational domain, between regions of emerging flux and the plage (the latter containing dynamic fibrils). In order to perform a comparison of the physics and the evolution of the observed spicule with those in the simulation, we focus on a particular region, i.e., x = [40, 45] Mm, where two neighboring spicules (hereafter "spicule 1" and "spicule 2") are seen to develop at a favorable angle with the LOS (e.g., Figures 6(a), (b), annotated and indicated with arrows), which results in well-isolated parabolic profiles in the various x-tplots of the synthetic observables presented in Figures 6(c)–(h). We assume that the spicule is not oriented in such a way that the LOS intersects it perpendicularly over its length, as the latter seems an extreme case for its orientation (likewise for the case where the spicule is viewed along its axis). Thus, the geometry in the model seems reasonable for the interpretation of the observations.

We computed synthetic ALMA/Band6 observations from our simulations at a single wavelength position of $\lambda = 1.2$ mm. For this, we used the LTE module of the Stockholm Inversion Code (de la Cruz Rodríguez et al. 2016; de la Cruz Rodríguez 2019). It computes the partial densities of all species considered in the calculations using the electron densities and gas pressure stratifications from the simulation. For the construction of the equation of state (EOS) we used the first 28 elements of the periodic table with three ionization stages, except for H. For H we used a simplified EOS that only included H₂ molecules. Many of those elements do not contribute at mm wavelengths, but they are included in the opacity and the background opacity (for the latter we considered partial densities only for elements that are major contributors). Continuum opacities were calculated using routines ported from the ATLAS code (Kurucz 1970), which include the main opacity source at mm wavelengths (free-free hydrogen absorption; e.g., see Wedemeyer et al. 2016). We also note that free-free and bound-free opacity processes from H and H were included in addition to those for the other atoms considered. Emergent intensity was calculated using a formal solver of the unpolarized radiative transfer equation based on cubic Bezier splines (Auer 2003; de la Cruz Rodríguez et al. 2013). The viewing geometry chosen was of

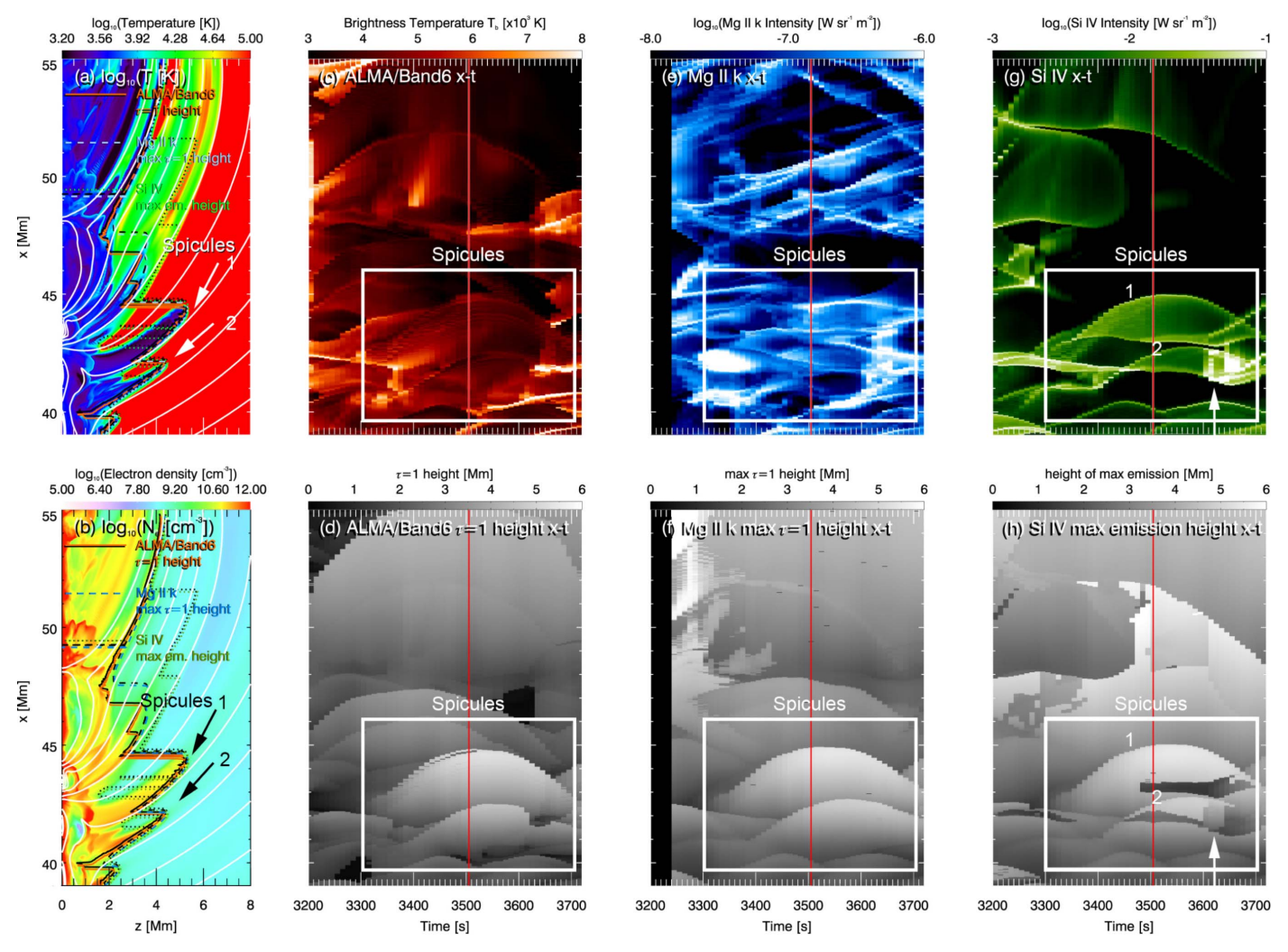


Figure 6. Synthetic x–t plots from the Bifrost simulation showing spicules 1 and 2. The leftmost panels show a snapshot from the simulation at t = 3500 s for (a) $\log_{10} T$ and (b) $\log_{10} N_e$. Upper panels (c), (e), and (g) show x–t in ALMA/Band6 T_b (in red), Mg II k (in blue), and Si IV (in green) synthesized intensities, respectively. Bottom panels (d), (f), and (h) present x–t plots for the geometric height with $\tau = 1$ for ALMA/Band6, the maximum $\tau = 1$ height for the wavelength-integrated Mg II k, and the height of maximum emission for Si IV. Boxed areas denote the regions of spicules (best seen in Si IV) and the plage. With a red line in the x–t plots we mark the time shown in panels (a) and (b).

an "observer" looking "top-down" the domain (i.e., assuming a LOS along the vertical direction in the simulation). We show the ALMA/Band6 *x*–*t* plot in Figure 6(c).

In order to synthesize the Mg II k line emission from the simulated spicules we used the RH radiative transfer code (Uitenbroek 2001; Pereira & Uitenbroek 2015). The synthesis was done individually for each vertical column of the simulation domain, for an observer looking "top-down" the simulated box (i.e., the *z*-axis in Figures 6(a), (b)). We show an x-t plot in Figure 6(e) made after integrating Mg II k in a wavelength range of $\Delta\lambda=0.7$ Å centered at the k3 rest wavelength of 2796.35 Å.

Lastly, we computed the Si IV 1393 Å spectrum assuming ionization equilibrium and optically thin emission. From the spectrum we computed the intensity by integrating the locally determined emissivity along the same LOS as before. We thus produced full spectra, which can be used for comparison to the IRIS Si IV 1393 Å rasters. An illustration of the Si IV synthesis is provided as an x-t plot in Figure 6(g) (in this example, we provide the total intensity of Si IV 1393 Å).

Furthermore, for the optically thick synthetic observables (i.e., Mg II k, ALMA/Band6), we used the height where the

optical depth $\tau = 1$ as a function of λ to interpret the diagnostic information we got from the IRIS Mg II k and ALMA/Band6 optically thick observations. This quantity is commonly referred to as the formation height of a line. For demonstration purposes, here we show the maximum $\tau=1$ height that Mg II k has formed for the wavelength range $\Delta \lambda = 0.7 \text{ Å from its rest wavelength position (Figure 6 (f))}.$ Note that in our discussion we also make use of the $\tau = 1$ height at specific wavelength positions (more in Section 4). The Mg II k line typically includes three components: k2v and k2r form in the wings and originate from the low chromosphere, whereas k3, often in absorption, forms in the upper chromosphere. Conversely, Figure 6(f) shows that the integrated Mg II k probes the various structures at a range of geometric heights below that maximum $\tau = 1$ height (i.e., it is an upper limit), while ALMA/Band6 roughly observes the spicular plasma at consistently greater heights than those of the wavelengthintegrated Mg II k observable (more in Section 4).

The optically thin Si IV synthetic observable captures the basic qualitative behavior of the x-t plot from the observations (Figure 5; green-colored plot), in that it tends to highlight the parabolic profile of spicules 1 and 2. We expand on the

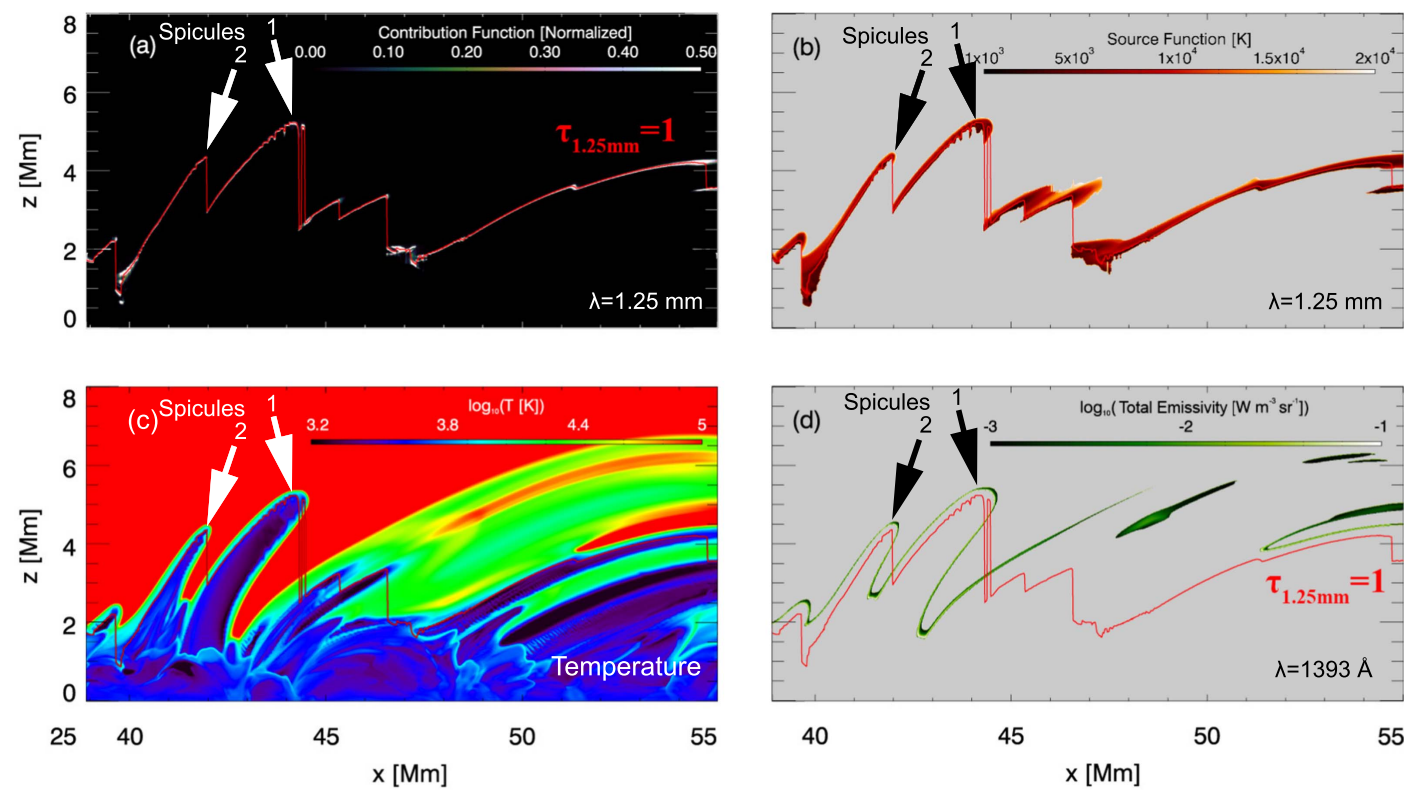


Figure 7. ALMA/Band6 1.25 mm synthesis from the time of the snapshot of the simulation in Figure 6 of (a) the normalized contribution function (i.e., g_{ν} / max(g_{ν}), clipped between 0.0 and 0.5, linear scale) and (b) the related source function, S_{ν} (here expressed in units of temperature (K) and shown only for regions where $g_{\nu}/\max(g_{\nu}) \geqslant 10^{-4}$; gray mask). The red line in all panels shows the ALMA/Band6 $\tau = 1$ height. (c) Temperature map. (d) Color contour (in green; logarithmic scaling; gray mask clipping low values) of the total emissivity, η , for Si IV 1393 Å. Note the close correspondence in geometric heights for the total emissivity of Si IV 1393 Å and $\tau = 1$ for ALMA/Band6.

similarities seen between the synthetic observables and the observations in the next section (Section 4). Intensities in ALMA/Band6 and Mg II k seem to almost always originate from below that Si IV "envelope," with ALMA/Band6 intensities extending closer to that Si IV envelope than Mg II k. These diagnostics are formed in a region with very strong gradients and very rapid temporal evolution. This means that even though they may be formed in close proximity, they can still be substantially different. To illustrate this point better, we calculated the geometric height of maximum emission for Si IV, and we show the resulting *x*-*t* plot in Figure 6(h). As for the Mg II k line, it forms over a broad range of heights—we discuss its diagnostic information in comparison to the other observables in Paper II.

In Figure 7(b) we present the ALMA/Band6 source function, S_{ν} , calculated separately at each column in the simulated domain, and in Figure 7(a) we present the resulting contribution function, g_{ν} :

$$g_{\nu} = S_{\nu} e^{-\tau_{\nu}} \alpha_{\nu} = g_{\nu}(N_{\rm e}, T) \tag{3}$$

where α_{ν} is the monochromatic absorption coefficient and τ_{ν} is the optical depth for $\nu=240~\mathrm{GHz}$ ($\lambda=1.25~\mathrm{mm}$). The source function shows at each column in the domain the range of geometric heights where the (optically thick) ALMA/Band6 free–free emission forms. The synthetic ALMA/Band6 spectral intensity, I_{ν} , was obtained by integrating the contribution function over the geometric heights along the LOS, z, as

follows:

$$I_{\nu} = \int g_{\nu} dz = \int S_{\nu} e^{-\tau_{\nu}} \alpha_{\nu} dz. \tag{4}$$

Pairing the above Equation (4) with the Rayleigh–Jeans approximation of Equation (2), we get a map for brightness temperatures, $T_{\rm b}$. For comparison, in Figure 7(d) we show a map of the total (i.e., wavelength-integrated) emissivity for Si IV 1393 Å, $\eta = \int \eta_{\nu} c/\lambda^2 d\lambda$, with the geometric height where ALMA/Band6 $\tau = 1$. This shows that the total intensity from Si IV,

$$I = \int \eta dz \tag{5}$$

(x-t plot of Figure 6(g)), may be coming from different geometric heights in the solar atmosphere along the LOS (being optically thin)—but still delineating the spicules—while the ALMA/Band6 optically thick emission comes from a similarly corrugated $\tau=1$ height (but locally within a small width from that $\tau=1$ line; Figures 7(a), (b)), following closely the height variation of Si IV total emissivity (panel (d)). Figures 7(c) and (d) demonstrate that ALMA/Band6 provides the temperature at the top part and along the spicules. As for the Mg II k line (not shown in this plot), it forms over a broad range of heights, so for reasons of clarity we do not show a $\tau=1$ line in this figure. Its formation height has strong wavelength dependence as we show in the next section (Section 4). We discuss the diagnostic information from Mg II k with $\tau=1$ geometric heights at

different wavelength positions in comparison to the formation height of the other observables for spicules in Paper II (morphology model).

4. Results

The analysis in the previous sections and the qualitative comparison between observational and synthetic *x*–*t* plots reveal that our joint IRIS and ALMA observations have likely captured a Type II spicule observed on-disk. Figure 4 provides strong evidence of the spicule's RBE signatures along its slender structure. Also, the dynamic evolution is characterized by upward and downward motions projected in the plane of the sky (e.g., the parabolic profile in Figure 5) as also typically seen even for spicules at the limb. Here, we discuss the similarities in the dynamics of the spicules between the synthetic observables and the observations.

To address the similarities with respect to the dynamic evolution of the spicules, we produced a set of x-t plots at different wavelength positions for the simulated region of spicules (Figure 8) to compare them against the *x*–*t* plots from the IRIS and ALMA/Band6 observations presented in Figure 5. In addition, we degraded the spatial resolution of the synthetic observables via convolution with the appropriate 2D Gaussian kernel to match the observed ALMA/Band6 beam size (we picked a "worst" beam size value of 0.78) and the spatial resolution of the observed IRIS rasters (0."16 pix⁻¹ along the slit). Also, we produced wavelength-integrated x-tplots as done in Figure 5. The qualitative similarities seen in this comparison are striking. We note, however, that the signatures of spicule 2 are not as clear, perhaps because it is adjacent to spicule 1; therefore it is not seen against a dark background like spicule 1.

Regarding ALMA/Band6, we can see the increase of T_b at the onset of growth of spicule 1 at (x, t) = (2 Mm, 3300 s) and of spicule 2 around (x, t) = (1 Mm, 3300-3400 s) (displaysaturated at $T_b = 6000 \,\mathrm{K}$). In the observations (Figure 5), a similar increase in $T_{\rm b}$ can be seen to develop at the onset of growth at \sim 16:10 UT. Later, at the moment of network jet–like brightening in the simulation at (x, t) = (2 Mm, 3650 s), we see an enhancement in T_b (same (x, t) coordinates). Even though in the observations the network jet occurred during the calibration gap between ALMA/Band6 scans 13 and 16, there is evidence that a temperature enhancement was still ongoing at (x, t) = (3'', 16:19 UT). Note, however, that we are comparing the observations to events in simulation that is not meant to simulate a specific event; therefore differences might exist in the details of the simulation, namely, the amount of current, the field configuration, etc. Also, the range of values for the synthesized ALMA/Band6 T_b for each of the simulated spicules is about 2000 K lower than the observed ALMA/ Band6 temperatures in the spicules, suggesting that the energy balance in the simulations did not fully capture all the relevant processes (radiation, heating, ionization, etc.).

To identify the geometric heights where Mg II emission formed in our simulation we used an x-t plot of $\tau = 1$ heights as a function of wavelength (Figure 8; each x-t located at a specific wavelength and arranged in velocity space). We also plotted the parabolic profile for spicules 1 and 2 (yellow and green dotted lines) as taken from the corresponding $\tau = 1$ plots. We typically see that the spicules first appear in blueshifts (as high as $-37 \, \mathrm{km \ s^{-1}}$), which is consistent with the ascending phase in their evolution. Indications of RBE

effects are seen in the initial growth phase of the spicules in both Si IV and Mg II k (see blue oval at $-25 \,\mathrm{km \ s^{-1}}$ for spicule 1 and at $-12 \,\mathrm{km \ s^{-1}}$ for spicule 2; compare the blue ovals against the red ovals to see the difference in intensities). Mg II k progressively samples the spicule at maximum elongation at the line rest wavelength ($+0 \,\mathrm{km \ s^{-1}}$) and in the receding phase of the spicules in the red wing (here, down to $+25 \,\mathrm{km \ s^{-1}}$). In the x-t from IRIS observations of Mg II k rest $-55 \,\mathrm{km \ s^{-1}}$ (shown in Figure 5), we also got a signal at the blue wing (x, t) = (0-3'', $16:10-16:20 \,\mathrm{UT}$).

However, while the x-t plots of $\tau = 1$ in Figure 8 suggest that we are observing the spicule as it grows, stalls, and recedes, (1) the Mg II k intensity is too weak and (2) the various contributors to the line too complex in the *x*–*t* plot to highlight a rough parabolic profile. We emphasize that this is very similar to what was observed. For instance, see areas indicated by arrows where intensity is low (due to absorption, as we show in the following sections). In the wavelength-integrated map of the Mg II k line, we do not see a full (or even partial) parabolic trace as well defined as those in ALMA/Band6 and Si IV. This is the case for both the observations (Figure 5) and the simulation. Despite that, during the time of the network jet in the simulation, we see a significant intensity enhancement at the Si IV rest wavelength all the way to the blue wing (i.e., the area inside the dotted circle at $-25 \,\mathrm{km \ s^{-1}}$) as well as indications of Mg II absorption in the red wing (arrow in dotted circle at $+12 \text{ km s}^{-1}$). Likewise, we see a similar enhancement from the Mg II k line core to the blue wing in the observed x-t (between times 16:17 and 16:20 UT).

The most striking resemblance between the simulation and the observations is found in Si IV x-t (Figure 8). High Si IV emissivity has been observed to emanate from around the tip of the spicule as it grows, until it reaches the apex of the x-t parabolic profile, where the emission is then seen mostly at the core of the line (De Pontieu et al. 2017b; Chintzoglou et al. 2018). Remarkably, a network jet brightening here also occurs during the descending phase of the x-t profile (dotted circle in selected panels in Figure 8), and the emission is seen in redshifts (all the way up to $+25 \text{ km s}^{-1}$), as discussed above. Interestingly, the network jet-like brightening appears in Mg II k in blueshifts and also at the rest wavelength of the line but as a dark feature in the +12 and $+25 \,\mathrm{km \ s^{-1}}$ line positions (compare the dotted circle and locations indicated by arrows). We explore this clear intensity depression (in Mg II) in the spicules as well as anticorrelations with Si IV and ALMA/ Band6 in Paper II.

To better illustrate the similarities of the spicules in the model and in the observations, we show in Figure 9(a) a tricolor combination of the x-t plots that summarizes the evolution seen in the observations and in the simulation in ALMA/Band6 (red), Mg II k, (blue; 0.7 Å integration), and Si IV (green; 0.2 Å integration). At the same time this allows us to assess the instantaneous spatial distribution of the heating along the spicular column. Areas where red, green, or blue colors produce "color blends" essentially illustrate the multithermality of the plasma. In Figure 9(a) we show the tricolor plot with the ALMA/Band6 data gap masking all observables. In panel (b) we show all available data together with annotations. The tricolor plot from the observations (Figures 9(a), (b)) agrees with the general evolution of simulated spicules 1 and 2 (Figure 9(c)). Initially (dashed oval A in Figure 9(b)), the observed spicular plasma only extends to

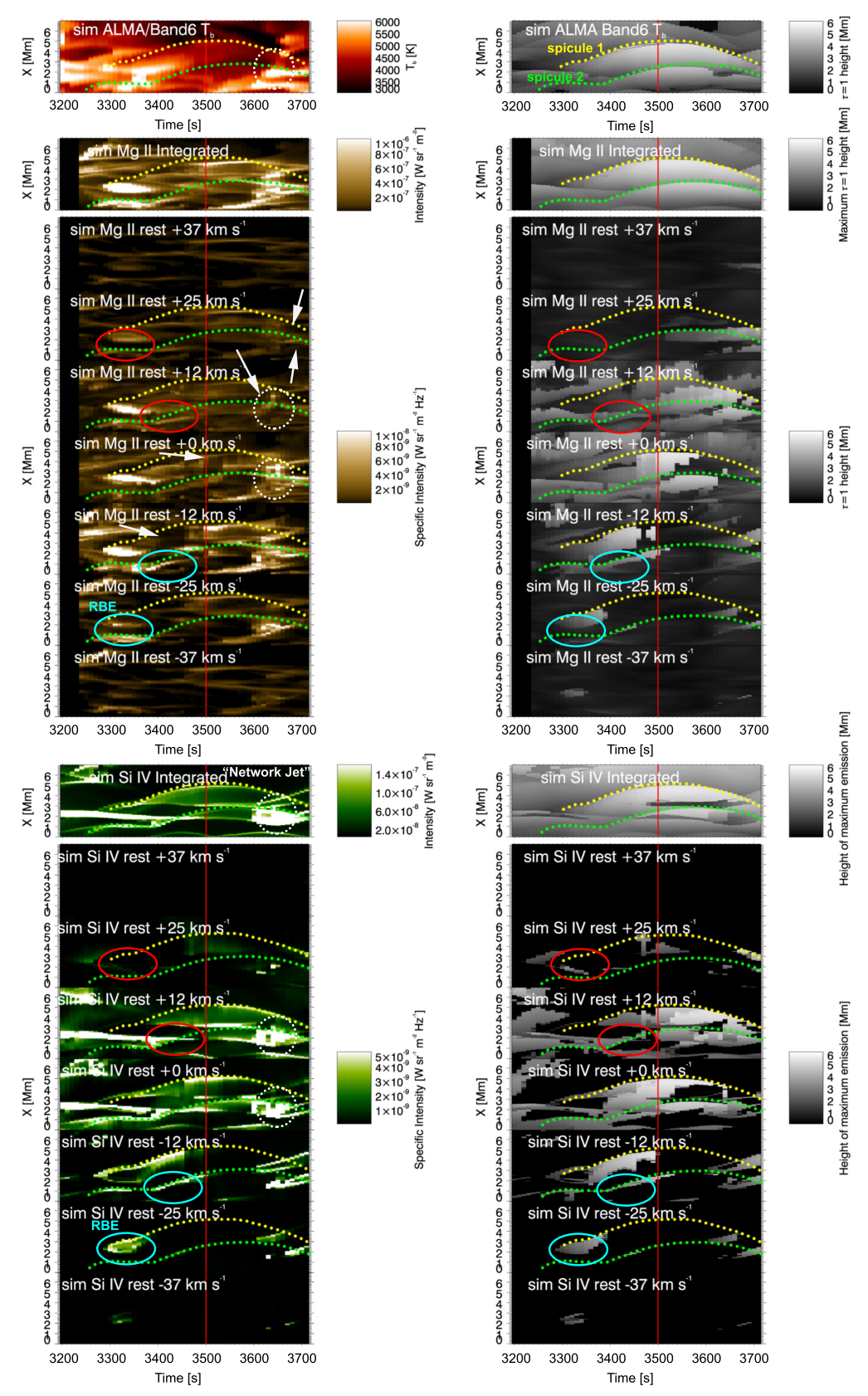


Figure 8. Left panels: x–t plots stacked along the wavelength (velocity space) for the synthetic observables produced from the simulation. Note the qualitative similarities to the x–t plots produced from the observations (Figure 5). Right panels: x–t plots of the height where τ = 1 for the optically thick observables and the height of maximum emission for the optically thin Si IV. Dotted lines highlight the parabolic profile of Type II spicules 1 and 2 (yellow and green colors, respectively). The arrows show locations of enhanced absorption in Mg II k. The ovals at ± 25 and ± 12 km s⁻¹ pinpoint locations with RBE signatures at the onset of spicule growth. The red vertical line marks the time shown in the previous plots.

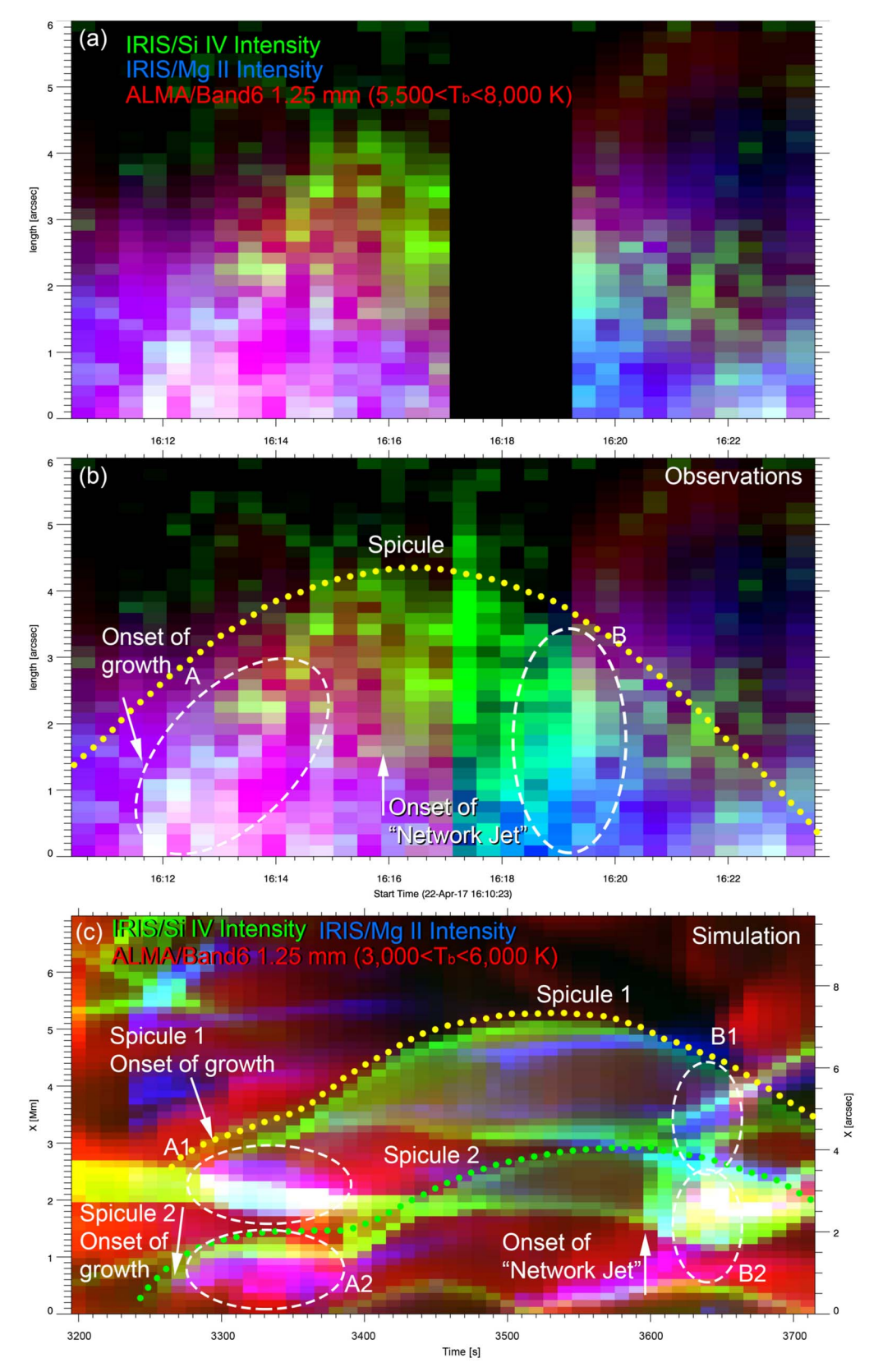


Figure 9. Panels (a) and (b): x-t plot combining observations shown in Figure 5 in a tricolor blend: IRIS Mg II (blue), Si IV (green), and ALMA/Band6 T_b (red). IRIS Mg II and Si IV are integrated along λ covering the line profiles. Panel (a) shows the ALMA/Band6 data gap by blocking the IRIS data. Panel (b) shows the IRIS data at all times. Initially the spicule is seen at low temperatures (magenta color blend). The white arrow marks the time of the sudden network jet brightening of the spicule in Si IV (suggesting $T \approx 80,000$ K). Note, however, that at the same time enhanced emission comes from spicular plasma at lower temperatures (e.g., ALMA $T_b \approx 8000$ K), suggesting that the spicule is a multithermal plasma structure. Panel (c): Similar plot from the corresponding synthetic observables for the simulated spicules of Figure 6. See text for discussion.

low heights and appears in relatively lower temperatures (no signal in Si IV emission; however, there is a signal in both ALMA/Band6 and Mg II k at the same location producing a magenta color blend). Eventually, the observed spicular plasma achieves higher temperatures (as also manifested by emission seen in Si IV raster scans; e.g., Figure 5), presumably due to heating from a shock traveling through the growing spicular column (thin "linear" bright trace in the x-t plots; Figures 9(a), (b)), which leads to both chromospheric and transition-region emission. Later on in the observations, shortly after the time when the spicule reaches its maximum elongation, the spicule seems to produce emission in all those wavelength ranges simultaneously. This is marked in Figure 9(b) with a white arrow as the onset of a network jet brightening. It is worth repeating here that while there is a data gap in ALMA/Band6 (dark gap in panel (a)), there are indications of high signals in ALMA/Band6 just after the end of the data gap (bright yellow color blend within dashed oval B). Eventually, as the spicule recedes, significant intensity is found in all three wavelength bands simultaneously (white color blend around 16:22 UT).

The behavior we saw in the observations is also seen in the synthetic tricolor plot for spicules 1 and 2 of Figure 9(c); i.e., there is significant intensity at the onset of spicule growth (white dashed ovals A1 and A2 containing regions with magenta colors), in addition to high emission in Si IV, which here is also seen to "envelop" the parabolic profile of the spicule at all times in the x-t plots. Within the time of the network jet brightening (occurring primarily in spicule 2 but also in spicule 1) high intensity is reached in all these wavelengths (areas within dashed ovals B1 and B2). Therefore, our synthetic observables (Figure 6) compared to the observations in Figure 5 support the multithermal nature of spicules (e.g., Chintzoglou et al. 2018, as revealed by VAULT2.0 and IRIS observations). However, as we mention above, the brightness temperatures for the spicule in the synthetic ALMA/Band6 observable are $\approx 2000 \,\mathrm{K}$ lower than $T_{\rm b}$ in the observations for either of the spicules.

The consideration of time-dependent ionization in the simulation has the effect of increasing the electron density (Carlsson & Stein 2002; Wedemeyer-Böhm et al. 2007) in chromospheric heights in the domain as compared to previous simulations that did not consider NEQ ionization effects (e.g., see Martínez-Sykora et al. 2020b). The above also suggests that, with higher electron densities in the chromospheric plasma, ALMA/Band6 (sensitive to free-free emission from chromospheric electrons) is probing spicules in optically thick emission that originates from greater heights due to the increased electron density. This can be seen in the $\tau=1$ height shown in Figure 7(d) (red line), which roughly delineates the contour of the spicules; alternatively, compare the parabolic profiles in the x-t plots of ALMA/Band6 and Si IV (Figures 6(c), (e)). As we already know from previous studies of spicules seen on-disk (e.g., Chintzoglou et al. 2018), Si IV emission from Type II spicules roughly demarcates the latter's linear extent as projected on the plane of the sky.

In addition, by including all these effects in the simulation, the simulated spicule 2 (and to some extent spicule 1) suddenly brightens along its full length, producing a network jet. The apparent (i.e., simulated plane-of-the-sky) speed of this network jet is $\approx 140 \, \mathrm{km \ s^{-1}}$, a speed more than three times the highest Doppler velocities contained in the synthetic spectra of the spicule at that time (and about six to seven times as high

as the bulk plasma speeds in the spicule, which at the time of the network jet are primarily downflows). This mismatch between apparent speeds and actual plasma speeds (revealed by RBE/Doppler velocities) supports the idea that some network jets can be rapidly propagating heating fronts (De Pontieu et al. 2017b; Chintzoglou et al. 2018), in contrast with other interpretations, e.g., rapid upward mass motions (Tian et al. 2014). The similarity between the model and the observations is quite striking and once again points to the impulsive heating and the multithermal nature of spicules (Chintzoglou et al. 2018).

5. Summary and Conclusions

In this work we focus on addressing the nature and the dynamics of chromospheric/transition-region jetlike features, i.e., Type II spicules, using high-time cadence and high-spatial resolution data from the ALMA and IRIS observatories. Our target was a plage region in the leading part of NOAA AR 12651. The spatial distribution of the plage region in the FOV allowed the simultaneous observation of regions of high chromospheric emission and regions with low background emission; the latter permitted the unambiguous on-disk observation of a spicule with ALMA/Band6 observations. Thanks to this favorable observing geometry, our analysis was free from many of the difficulties faced in previous works, such as low S/N and strong LOS superposition in the data, which is common in observations of spicules at the limb (e.g., Tei et al. 2020). In addition, to assist the interpretation of these unique observations, we employed a 2.5D numerical simulation (Bifrost model) of spicules that considered ambipolar diffusion in NEQ ionization conditions. We produced synthetic observables to compare the model with our observations from ALMA/Band6 and IRIS.

Our main findings can be summarized as follows:

- 1. We conclude that the dynamic linear structure captured in the common IRIS and ALMA/Band6 FOV is a Type II spicule. This is supported by (a) the slender profile of the structure, (b) the RBE in the spectrum of Mg II k and Si IV from the bulk of the structure (Figure 4), and (c) the dynamics seen in the spacetime plot (parabolic spacetime profile; Figure 5) in the observations and in the spacetime plots from the synthetic observables produced from the simulation (Figure 6).
- 2. The identified spicule experienced a network jet brightening (apparent speed of $\approx 95 \,\mathrm{km \ s^{-1}}$). Our synthetic observables (Figure 8) and observations (Figures 5 and 9) show clear agreement with each other, including the occurrence of a network jet brightening (in the simulation the apparent speed was $\approx 140 \text{ km s}^{-1}$). Note that the IRIS raster time cadence was 26 s, while the simulation's time cadence was 10 s, each imposing a lower limit on the deduced apparent speed. This apparent brightening in Si IV likely occurred due to a rapidly propagating heating front along the spicular mass, instead of representing rapid upward mass flows (consistent with De Pontieu et al. 2017b; Chintzoglou et al. 2018). In fact, both the observed and the simulated spectra show a clear red-blue asymmetry, suggesting mass motions directed away from the observer during the time of the network jet.
- 3. We confirm the multithermal nature of dynamic Type II spicules (Chintzoglou et al. 2018). The tricolor spacetime

- plot (combining ALMA and IRIS observables; Figure 9) reveals a picture strongly suggesting that spicular plasma emits at multiple temperatures simultaneously, also supported by the synthetic observables from the Bifrost simulation (Figure 6).
- 4. We also noted interesting intensity depressions, high-lighted in the Mg II k spacetime plots (i.e., in the observations in Figure 5 and in the simulation in Figure 8). We conclude that the apparent anticorrelation or lack of correlation (which may in part be due to observing different parts of the same events/structures as cospatial or even as non-cospatial owing to LOS projection effects) has its origin in Mg II opacity effects in plage structures. Strong absorption is the reason behind the low Mg II intensities emerging from greater geometric heights in the locations of spicules.

In a separate publication (Chintzoglou et al. 2021) we focus on the morphological similarities between plage structures seen in ALMA and IRIS observations, with an emphasis on the formation height of the optically thick free–free emission observed with ALMA/Band6.

This paper makes use of the following ALMA data: ADS/ JAO.ALMA#2016.1.00050.S. ALMA is a partnership of the European Southern Observatory (ESO; representing its member states), the National Science Foundation (NSF; USA), and NINS (Japan), together with NRC (Canada), MOST and ASIAA (Taiwan), and KASI (Republic of Korea) and in cooperation with the Republic of Chile. The Joint ALMA Observatory is operated by ESO, AUI/NRAO, and NAOJ. We gratefully acknowledge support by NASA contract NNG09FA40C (IRIS). J.M.S. is also supported by NASA grants NNX17AD33G and 80NSSC18K1285 and NSF grant AST1714955. V.H. is supported by NASA grant 80NSSC20K1272. J.C.d.l.R. is supported by grants from the Swedish Research Council (2015-03994), the Swedish National Space Board (128/15), and the Swedish Civil Contingencies Agency (MSB). This project has received funding from the European Research Council (ERC) under the European Union's Horizon 2020 research and innovation program (SUNMAG, grant agreement 759548). M.S., S.J., and S.W. are supported by the SolarALMA project, which has received funding from the ERC under the European Union's Horizon 2020 research and innovation program (grant agreement No. 682462), and by the Research Council of Norway through its Centres of Excellence scheme, project number 262622. The simulations and Mg II synthesis were run on clusters from the Notur project and the Pleiades cluster through computing projects s1061, s1630, and s2053 from the Highend Computing division of NASA. This research is also supported by the Research Council of Norway through its Centres of Excellence scheme, project number 262622, and through grants of computing time from the Programme for Supercomputing. IRIS is a NASA small-explorer mission developed and operated by LMSAL with mission operations executed at the NASA Ames Research Center and major contributions to downlink communications funded by the European Space Agency and the Norwegian Space Centre. HMI and AIA are instruments on board SDO, a mission for NASA's Living with a Star program.

ORCID iDs

Georgios Chintzoglou https://orcid.org/0000-0002-

1253-8882

```
Bart De Pontieu https://orcid.org/0000-0002-8370-952X
Juan Martínez-Sykora https://orcid.org/0000-0002-
0333-5717
Viggo Hansteen https://orcid.org/0000-0003-0975-6659
Jaime Cruz de la Rodríguez https://orcid.org/0000-0002-
4640-5658
Shahin Jafarzadeh https://orcid.org/0000-0002-7711-5397
Sven Wedemeyer https://orcid.org/0000-0002-5006-7540
Timothy S. Bastian https://orcid.org/0000-0002-0713-0604
Alberto Sainz Dalda https://orcid.org/0000-0002-
```

```
3234-3070
                              References
Auer, L. 2003, in ASP Conf. Ser. 288, Insight into Multi-Dimensional
   Transfer, ed. I. Hubeny, D. Mihalas, & K. Werner (San Francisco, CA:
   ASP), 405
Bastian, T. S., Chintzoglou, G., De Pontieu, B., et al. 2017, ApJL, 845, L19
Bose, S., Henriques, V. M. J., Joshi, J., & Rouppe van der Voort, L. 2019,
    A&A, 631, L5
Carlsson, M., & Stein, R. F. 2002, ApJ, 572, 626
Chintzoglou, G., De Pontieu, B., Martínez-Sykora, J., et al. 2018, ApJ, 857, 73
Chintzoglou, G., De Pontieu, B., & Martínez-Sykora, J. 2021, ApJ, 906, 83,
   (Paper II)
Cotton, W. D. 2017, PASP, 129, 094501
de la Cruz Rodríguez, J. 2019, A&A, 631, A153
de la Cruz Rodríguez, J., De Pontieu, B., Carlsson, M., &
   Rouppe van der Voort, L. H. M. 2013, ApJL, 764, L11
de la Cruz Rodríguez, J., Leenaarts, J., & Asensio Ramos, A. 2016, ApJL,
   830, L30
De Pontieu, B., Martínez-Sykora, J., & Chintzoglou, G. 2017b, ApJL, 849, L7
De Pontieu, B., McIntosh, S. W., Carlsson, M., et al. 2007, Sci, 318, 1574
De Pontieu, B., McIntosh, S. W., Carlsson, M., et al. 2011, Sci, 331, 55
De Pontieu, B., McIntosh, S. W., Hansteen, V. H., & Schrijver, C. J. 2009,
     pJL, 701, L1
De Pontieu, B., Title, A. M., Lemen, J. R., et al. 2014, SoPh, 289, 2733
Golding, T. P., Leenaarts, J., & Carlsson, M. 2016, ApJ, 817, 125
Gudiksen, B. V., Carlsson, M., Hansteen, V. H., et al. 2011, A&A, 531, A154
Henriques, V. M. J., Kuridze, D., Mathioudakis, M., & Keenan, F. P. 2016,
    ApJ, 820, 124
Iijima, H., & Yokoyama, T. 2017, ApJ, 848, 38
Klimchuk, J. A. 2012, JGRA, 117, A12102
Kurucz, R. L. 1970, SAOSR, 309
Langangen, Ø., De Pontieu, B., Carlsson, M., et al. 2008, ApJL, 679, L167
Leenaarts, J., Carlsson, M., Hansteen, V., & Rutten, R. J. 2007, A&A, 473, 625
Lemen, J. R., Title, A. M., Akin, D. J., et al. 2012, SoPh, 275, 17
Loukitcheva, M., Solanki, S. K., Carlsson, M., & White, S. M. 2015, A&A,
Martínez-Sykora, J., De Pontieu, B., Carlsson, M., et al. 2017, ApJ, 847, 36
Martínez-Sykora, J., De Pontieu, B., de la Cruz Rodriguez, J., &
   Chintzoglou, G. 2020a, ApJL, 891, L8
Martínez-Sykora, J., De Pontieu, B., De Moortel, I., Hansteen, V. H., &
   Carlsson, M. 2018, ApJ, 860, 116
Martínez-Sykora, J., Leenaarts, J., De Pontieu, B., et al. 2020b, ApJ, 889, 95
McMullin, J. P., Waters, B., Schiebel, D., Young, W., & Golap, K. 2007, in
   ASP Conf. Ser. 376, CASA Architecture and Applications, ed. R. A. Shaw,
   F. Hill, & D. J. Bell (San Francisco, CA: ASP), 127
Nóbrega-Siverio, D., Martínez-Sykora, J., Moreno-Insertis, F., & Carlsson, M.
  2020, A&A, 638, A79
Patsourakos, S., Klimchuk, J. A., & Young, P. R. 2014, ApJ, 781, 58
Pereira, T. M. D., De Pontieu, B., Carlsson, M., et al. 2014, ApJL, 792, L15
Pereira, T. M. D., & Uitenbroek, H. 2015, A&A, 574, A3
Pesnell, W. D., Thompson, B. J., & Chamberlin, P. C. 2012, SoPh, 275, 3
Rau, U., & Cornwell, T. J. 2011, A&A, 532, A71
Rouppe van der Voort, L., De Pontieu, B., Pereira, T. M. D., Carlsson, M., &
   Hansteen, V. 2015, ApJL, 799, L3
```

Rutten, R. J. 2017, A&A, 598, A89

Scherrer, P. H., Schou, J., Bush, R. I., et al. 2012, SoPh, 275, 207

Secchi, A. 1877, Structure du Soleil (Suite)—Activite Extérieure (Paris: Gauthier-Villars)
Shimojo, M., Bastian, T. S., Hales, A. S., et al. 2017, SoPh, 292, 87
Shimojo, M., Kawate, T., Okamoto, T. J., et al. 2020, ApJL, 888, L28
Skogsrud, H., Rouppe van der Voort, L., & De Pontieu, B. 2016, ApJ, 817, 124
Tei, A., Gunár, S., Heinzel, P., et al. 2020, ApJ, 888, 42
Tian, H., DeLuca, E. E., Cranmer, S. R., et al. 2014, Sci, 346, 1255711
Tripathi, D., & Klimchuk, J. A. 2013, ApJ, 779, 1
Uitenbroek, H. 2001, ApJ, 557, 389

Vourlidas, A., Beltran, S. T., Chintzoglou, G., et al. 2016, JAI, 5, 1640003 Wedemeyer, S., Bastian, T., Brajša, R., et al. 2016, SSRv, 200, 1 Wedemeyer, S., Szydlarski, M., Jafarzadeh, S., et al. 2020, A&A, 635, A71 Wedemeyer-Böhm, S., Ludwig, H. G., Steffen, M., Leenaarts, J., & Freytag, B. 2007, A&A, 471, 977 White, S. M., Iwai, K., Phillips, N. M., et al. 2017, SoPh, 292, 88 Wootten, A., & Thompson, A. R. 2009, IEEEP, 97, 1463 Yokoyama, T., Shimojo, M., Okamoto, T. J., & Iijima, H. 2018, ApJ, 863, 96